

Article

Green Synthesis of Manganese-Cobalt Oxyhydroxide Nanocomposite as Electrocatalyst for Enhanced Oxygen Evolution Reaction in Alkaline Medium

Rajeh Alotaibi ^{*,†} , Mabrook S. Amer [†] , Prabhakarn Arunachalam ^{*}  and Saad G. Alshammari 

Chemistry Department, College of Science, King Saud University, P.O. Box 2455, Riyadh 11451, Saudi Arabia; msamer@ksu.edu.sa (M.S.A.); salshammari@ksu.edu.sa (S.G.A.)

^{*} Correspondence: raalotaibi@ksu.edu.sa (R.A.); parunachalam@ksu.edu.sa (P.A.); Tel.: +966-114696026 (P.A.)

[†] These authors contributed equally to this work.

Abstract: Using green synthetic methods, a manganese-cobalt oxyhydroxide (MnCo-OOH) nanocomposite for electrocatalysis was prepared. Electrocatalysts were examined using powder X-ray diffraction analysis (XRD), Fourier transform infrared spectroscopy (FT-IR), and field-emission scanning electron microscopy (FESEM). In an alkaline medium, cyclic voltammetry and chronoamperometric analysis were applied to assess the electrocatalytic features of the MnCo-OOH nanocomposite. A strong correlation existed between MnCo-OOH's morphology, crystallinity, and electrochemical activity. Upon examining the electrochemical characteristics, the as-deposited MnCo-OOH catalyst demonstrated a significantly lower overpotential, achieving $75 \text{ mA} \cdot \text{cm}^{-2}$ OER current density at 370 mV, four times larger than $19.7 \text{ mA} \cdot \text{cm}^{-2}$ for CoOOH catalysts, signifying that the MnCo-OOH catalyst exhibits a higher electrocatalytic OER features. In addition, the MnCo-OOH nanocomposite demonstrated a high current density of 30 and $65 \text{ mA} \cdot \text{cm}^{-2}$ at 1.55 and 1.60 V_{RHE} for 12 h in 1.0 M KOH aqueous electrolyte. As a result of this study, it was determined that the fabricated MnCo-OOH nanocomposite would be an appropriate electrocatalyst in water electrolysis.

Keywords: cobalt oxyhydroxide; green synthesis; oxygen evolution reaction; electrocatalysts



Citation: Alotaibi, R.; Amer, M.S.; Arunachalam, P.; Alshammari, S.G. Green Synthesis of Manganese-Cobalt Oxyhydroxide Nanocomposite as Electrocatalyst for Enhanced Oxygen Evolution Reaction in Alkaline Medium. *Catalysts* **2024**, *14*, 369. <https://doi.org/10.3390/catal14060369>

Received: 16 May 2024

Revised: 31 May 2024

Accepted: 2 June 2024

Published: 6 June 2024



Copyright: © 2024 by the authors. Licensee MDPI, Basel, Switzerland. This article is an open access article distributed under the terms and conditions of the Creative Commons Attribution (CC BY) license (<https://creativecommons.org/licenses/by/4.0/>).

1. Introduction

Globally, alternative energy sources as well as sustainable energy storage and conversion have been highly active topics of research [1,2]. A major focus of research is finding ways to reduce our dependence on fossil fuels and developing more efficient and renewable energy sources [3,4]. For electronic devices and vehicles, molecular hydrogen is proposed as a primary energy storage medium [1,5]. Moreover, the transportation sector needs energy-efficient storage technologies and environmentally friendly charging systems. Electrochemical water splitting limitations can be overcome by cheap and reliable electrochemical methods [6,7]. The thermodynamically unfavorable oxygen evolution reaction (OER) is a key issue for electrochemical water splitting. Hence, it is highly imperative to develop OER electrocatalysts with improved water oxidation kinetics and reduced overpotential to enhance energy conversion.

As of yet, no electrocatalytic material has reached the equilibrium potential of 1.23 V_{RHE} [8,9], which corresponds to the minimum reaction energy. Furthermore, noble metal oxides (e.g., IrO_2 and RuO_2) are needed electrode materials for acidic environments owing to their admirable electrochemical properties [10]. Commercially, electrocatalytic water splitting is not feasible because of high prices and scarcity of electrocatalysts. As a result, efficient, robust, and cost-effective non-noble metal electrochemical OER catalysts are essential. Recently, nanostructured materials found on earth have gained attention for applications in catalysis, sensing, and energy conversion [11–17]. As a result, bare metal oxide electrocatalytic performances toward OER were relatively low, with

$\text{NiO}_x > \text{CoO}_x > \text{FeO}_x > \text{MnO}_x$ [18]. Despite this, it appears that alloying influences, such as the integration of multiple active alloy elements, can promote OER performance [19,20]. In recent years, cobalt oxyhydroxide (CoOOH) has drawn the greatest attention as a heterogeneous catalyst among cobalt-containing materials [21]. There is a high electron transfer rate, multiple surface active sites, a large number of phase reactions, and extensive presence on the Katanga Copperbelt [22]. Further, CoOOH occurs naturally as a stable and multifunctional material and has been engaged as a CO sensor [23], can serve as an electrode candidate for energy storage systems, and can be applied as a super-capacitor [24–26]. Recently, researchers discovered that integrating a different transition metal into bimetallic CoO_x might enhance its intrinsic OER properties [27,28]. Several recent research reports have shown that mixed metal oxides and hydroxides form CoFe [29], NiFe [30,31], NiFeCo [32], and NiFeCoCe [33] electrocatalysts materials that can be used for electrocatalytic OER. In particular, the incorporation of transition metal ions over cobalt oxides/hydroxides is attractive to OER. Often, these transition metal ions are used in OER processes as catalysts to increase efficiency and reduce energy consumption.

It is traditional to synthesize metal oxide nanoparticles by first reducing them with a strong base, followed by a capping or reducing agent. It is sometimes necessary to dissolve these capping agents in organic solvents. It is also likely to reduce unnecessary toxic chemicals by using a green synthesis approach [34]. The green synthesis method uses plant-derived metabolites to synthesize metal oxide nanoparticles [35]. As a result of coating metal oxide nanoparticles with these metabolites, they are resistant to extensive aggregation and produce tunable particle sizes and well-defined morphologies [36]. Since plants contain diverse phytochemical profiles, the choice of plant species and their individual parts determines NP morphology and particle size [37]. Thus, green synthesis provides a cost-efficient and eco-friendly alternative to conventional nanoparticle synthesis. In addition, manganese with cobalt hydroxide can have synergistic effects leading to enhanced activity as a result of charge transfer between the metal and substrate.

Herein, we demonstrate manganese-doped cobalt oxyhydroxide catalysts using a green synthesis method using alkanna root extract as an electrocatalyst in alkaline media, followed by studies on electrocatalysis of OER reactions. Through FT-IR, XRD, N_2 sorption, and microscopic analysis, we determined the structural and textural features of the Mn-incorporated CoOOH electrocatalysts. As a result, the Mn-promoted CoOOH electrodes (surface area $75 \text{ m}^2/\text{g}$) were significantly more efficient than Mn or CoOOH electrodes and analogous to benchmark IrO_2 electrodes in terms of their onset potential shifting by 98 mV, small Tafel slope, and reduced charge transfer resistance. Due to their facile synthesis, characteristic structure, and remarkable electrocatalytic features, these ternary-based electrocatalysts could be used in industrialized water splitting.

2. Results and Discussion

2.1. Crystalline, Structural, and Surface Features of Mn-CoOOH

The manganese-incorporated CoOOH catalysts were obtained by green synthetic approach with an alkanna plant root extract. Figure 1 reveals the different phases for the development of crystalline manganese-incorporated CoOOH catalysts. The acquired material was cleaned with DI water several times to eliminate the impurities. In the final step, the resulting products were obtained by thermosetting processes to obtain the formation of MnCo-OOH materials.

Figure 2a displays the powder diffraction patterns of MnCo-OOH materials compared to CoOOH and $\text{Mn}(\text{OH})_2$. As displayed in Figure 2a, the CoOOH and MnCo-OOH catalysts show the characteristic CoOOH trigonal PXRD pattern (PDF # 01-073-0497). The sharp diffraction lines clearly indicate a relatively higher crystallinity for these products. For reference, the bare $\text{Mn}(\text{OH})_2$ catalysts showed the characteristic $\text{Mn}(\text{OH})_2$ hexagonal powdered XRD pattern (PDF # 01-073-5018). Additionally, Figure 2a displays the diffraction patterns of the MnCo-OOH electrodes that match the diffraction lines of CoOOH and $\text{Mn}(\text{OH})_2$ (PDF # 01-073-0497 and 01-073-5018, respectively). During the green synthetic process, no

other XRD peaks were observed, suggesting there were no crystalline phases. Overall, the results confirm that the synthetic process is successful in forming MnCo-OOH.

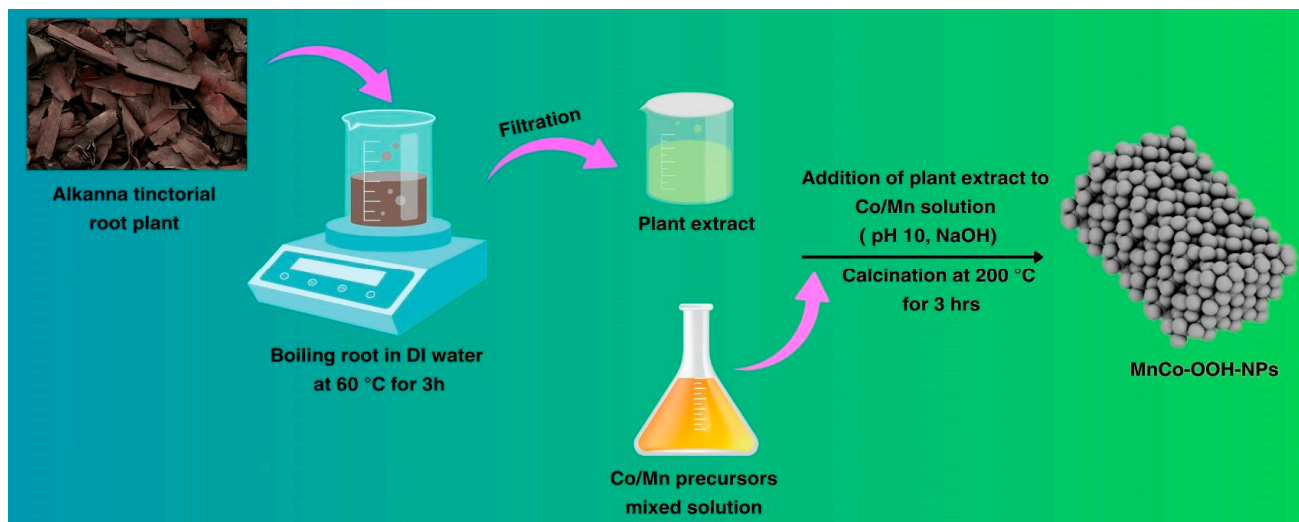


Figure 1. Schematic depiction of the fabrication of MnCo-OOH electrocatalysts obtained with alkanna plant root extract.

A comprehensive FTIR study was conducted on MnCo-OOH, CoOOH, and Mn(OH)₂ samples, varying from 4000 to 400 cm^{−1}, respectively. CoOOH materials exhibit a solid peak (Figure 2b) due to stretching vibrations of hydrogen-bound O-H groups [38,39], ν (O-H). There were two signals at (1613 cm^{−1} and 583 cm^{−1}) in CoOOH that were related to vibrations of the double and single bonds between Co and O, respectively [40]. The FTIR spectrum of the Mn(OH)₂ sample (Figure 2b) showed two strong peaks (612 and 502 cm^{−1}) originating from the stretching vibrations of Mn-O and Mn-O-Mn bonds [41], which indicate that MnO was formed. As Mn elements are introduced, vibrational modes shifted marginally to the lower wavenumber region. There were two distinctive M-O stretching vibration bands at 577 cm and 656 cm^{−1}. Hydrogen bonds between hydroxides of layers, interlayer water, and anions in the interlayer gap also contribute to this broad feature of the hydroxyl band. In addition, there was a weak distinctive band at 1613 cm^{−1}, related to the HOH-bending frequencies of adsorbed water molecules. It was verified by these FTIR results that MnCo-OOH catalysts can be produced effectively.

BET N₂ sorption isotherms were used to regulate the pore size and specific area of the nanomaterials. As shown in Figure 2c, MnCo-OOH and CoOOH, as well as Mn(OH)₂ nanomaterials have different BET isotherms. The BET specific area values of Mn(OH)₂, CoOOH, and MnCo-OOH were evaluated to be 87.48, 104.19, and 75.84 m²/g, respectively. Table 1 summarizes the BET results of fabricated materials. In accordance with IUPAC classifications, the N₂ sorption curves closely resemble type-IV isotherm hysteresis loops. It was detected at a relative pressure of greater than 0.7 that hysteresis loops were distinct, indicating capillary condensation of mesopores [42,43]. Based on BJHs, PSD curves were calculated for each fabricated material (Figure 2d). The pore sizes of these samples were 3.0 to 10 nm. As shown in Table 1, all samples had similar textural parameters such as pore volume, specific area, and diameter. The mesoporosity of the material can be attributed to its thermal decomposition, which could lead to weight loss and volume shrinkage. This characteristic of MnCo-OOH samples provides easy access for ions to electrode/electrolyte interfaces, allowing surface redox reactions to occur.

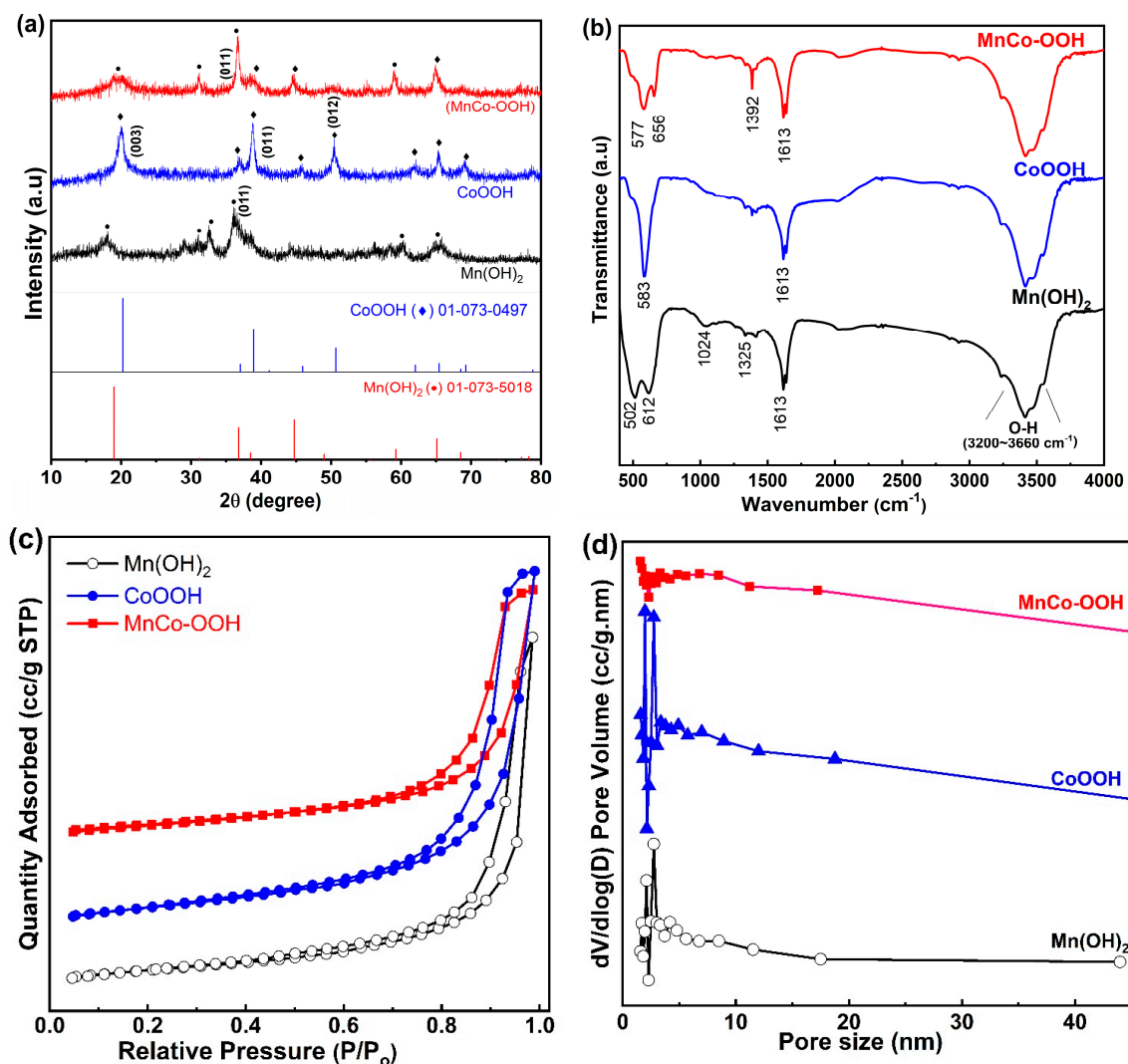


Figure 2. (a) The XRD patterns for pure CoOOH, Mn(OH)₂, and MnCo-OOH catalysts shown below are indexed using reference peaks; trigonal phase CoOOH (JCPDS # 01-073-0497), hexagonal Mn(OH)₂ (JCPDS # 01-073-1604), all the peaks are indexed via standard peaks, (b) FTIR patterns of pure CoOOH, Mn(OH)₂, and manganese incorporated CoOOH catalysts prepared by the green synthetic approach using alkanna plant root extract, (c) N₂ sorption isotherms, and (d), its agreeing BJH desorption pore size distributions of CoOOH, Mn(OH)₂, and MnCo-OOH catalyst.

Table 1. Textural properties of specific surface area, total pore volume, and the pore size of the MnO, MnCo-OOH, and CoOOH catalysts derived from nitrogen adsorption and desorption data.

Materials	Surface Area (m ² /g)	Pore Size (nm)	Pore Volume (cc/g)
Mn(OH) ₂	87.49	2.74	0.471
MnOCoO	75.84	1.60	0.337
CoO	104.20	1.96	0.484

The morphology and fine structure of CoOOH, Mn(OH)₂, and MnCo-OOH catalysts were evaluated using electron microscopy measurements (FESEM/HRTEM). Particularly, the stepwise pyrolysis in the air is exposed to maintain nanoparticle structure. FESEM images of the annealed in air CoOOH materials (Figure 3a,b) clearly show interconnected nanoparticles. Figure 3b shows high-resolution images of CoOOH nanoflakes. Further, it illustrates the morphology of assembled microblocks of nanoparticle aggregates with mean

particle sizes ranging from 15 to 30 nm. As a comparison, Figure 3c,d shows that $\text{Mn}(\text{OH})_2$ nanoparticles had a flower-like morphology and spherical shapes. High magnification SEM images (Figure 3d) clearly show that microplates of different sizes were stacked together. There was no noticeable change in the morphology of nanoflake CoOOH films after incorporating manganese (Figure 3e,f). According to Figure 3f, the incorporation of Mn into CoOOH nanoparticles hampers the agglomeration of nanoparticles, resulting in smaller particle sizes than bare CoOOH nanoparticles. Furthermore, we observed nanoflakes and spherical nanoparticles that provided electrode materials with more reaction sites. Further examination of the morphology of the CoOOH , $\text{Mn}(\text{OH})_2$, and MnCo-OOH NP catalysts was performed using TEM. As can be seen in Figure 4a,b, CoOOH is largely composed of hexagonal plates with smaller irregularly shaped particles. Figure 4c,d show that the bare $\text{Mn}(\text{OH})_2$ consists largely of ultra-small nanoplate-like structures with numerous small pores between the particles. Figure 4e,f illustrate that the MnCo-OOH composite material consists of hexagonal plates that are fused together in nanoaggregates, forming continuous networks. Additionally, the TEM image of MnCo-OOH clearly shows that the flakes have multiple interconnected nanoparticles and, therefore, several pores between them.

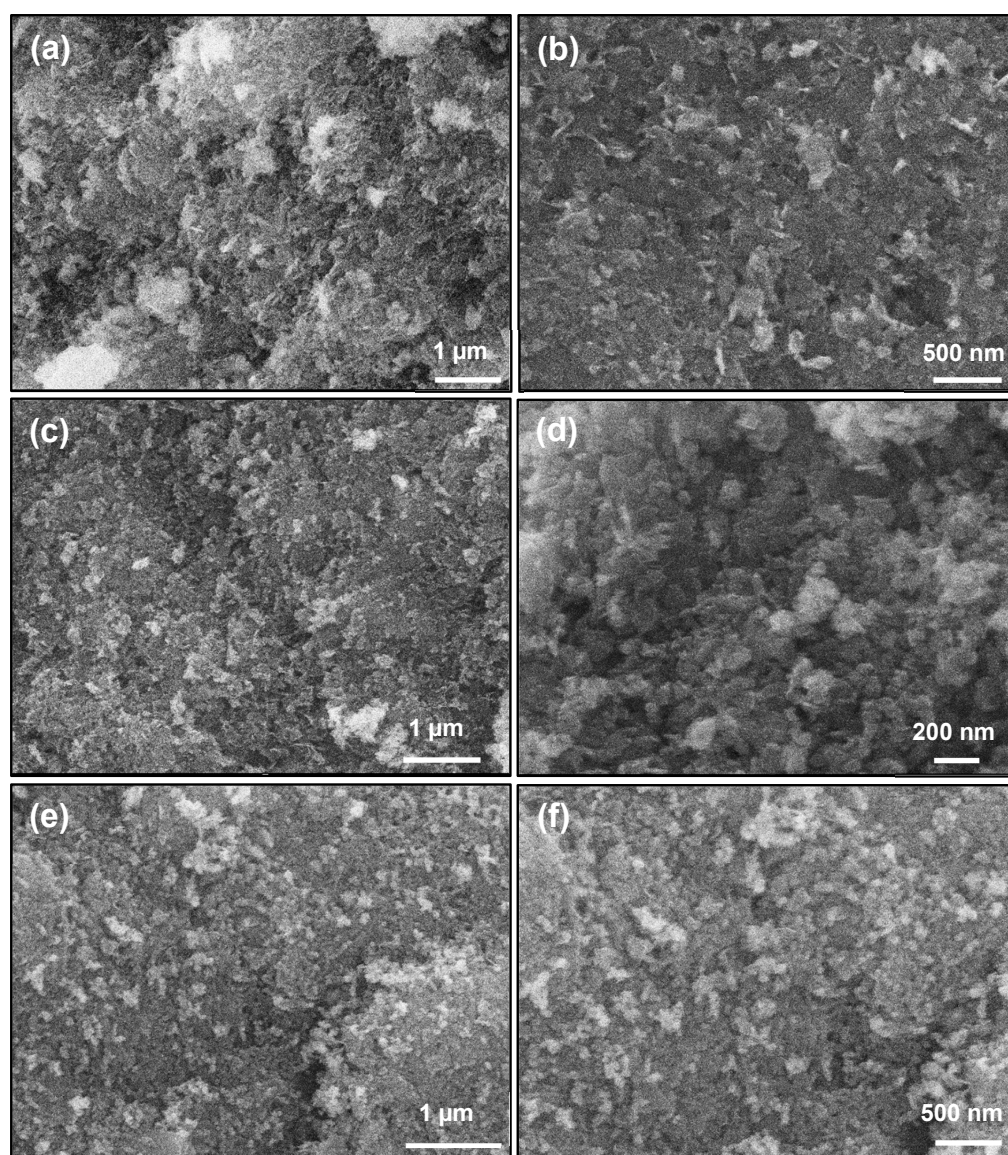


Figure 3. Morphological characteristics of samples. FE-SEM photographs of the obtained (a,b) CoOOH , (c,d) $\text{Mn}(\text{OH})_2$, and (e,f) MnCo-OOH samples.

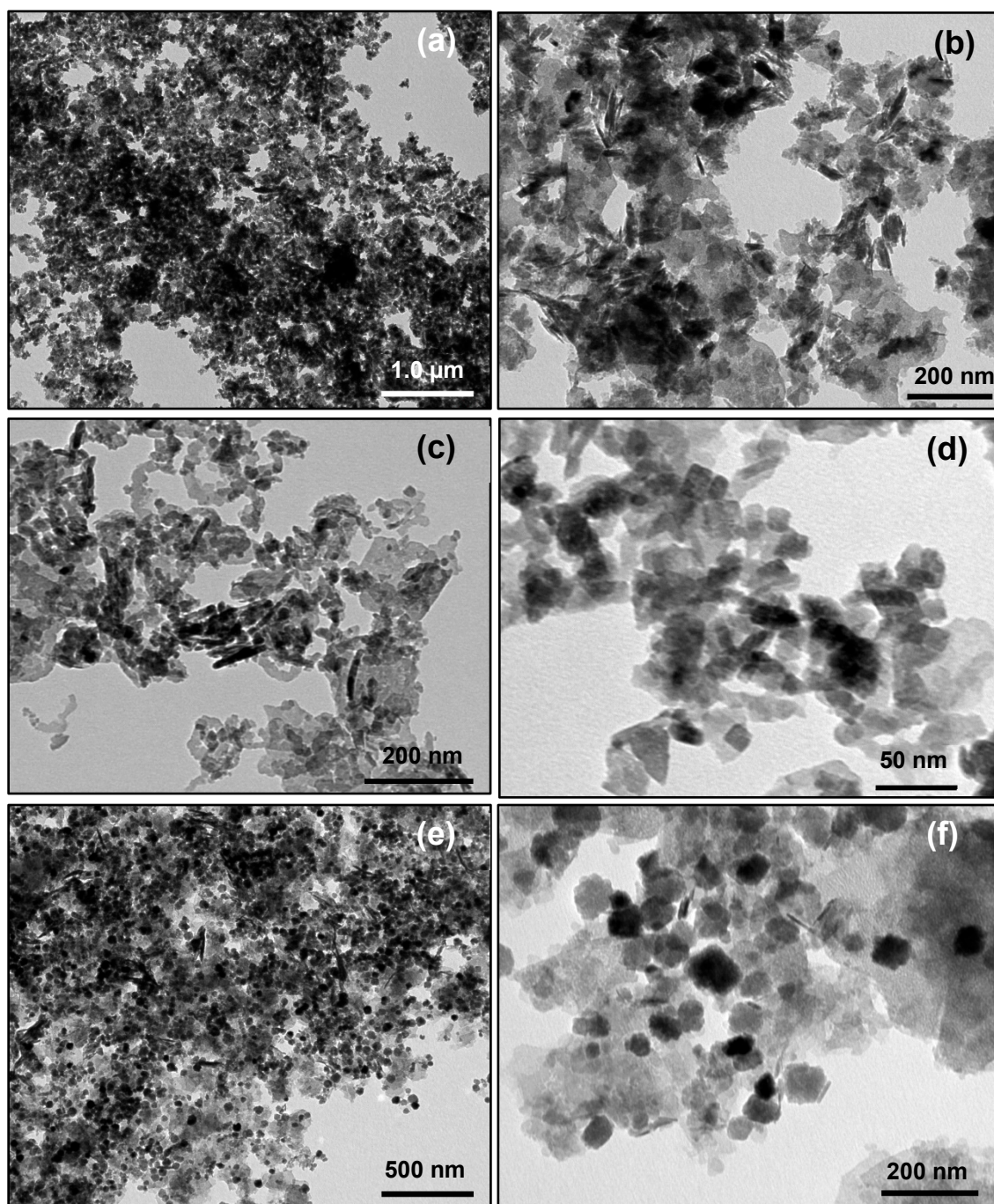


Figure 4. TEM analysis of CoOOH, Mn(OH)₂, and Co-Mn-OOH samples. TEM photographs of crystalline Co-OOH at different amplifications, (a,b) and Mn(OH)₂ samples at different amplifications (c,d), and MnCo-OOH (e,f) samples obtained through a green synthetic approach via alkanna tinctorial root extract.

Using energy-dispersive X-ray spectroscopy (EDAX), Mn loading in catalysts was evaluated. A detailed examination of EDAX mapping revealed the attendance of Mn, Co, and O components across the entire MnCo-OOH structure (Figure 5a–g). The EDAX mapping of CoOOH materials showed a homogenous distribution of Mn, Co, and O elements. Based on the EDAX analysis, MnCo-OOH catalysts consist of 7.61, 72.61, and 19.72 wt%, individually, for Mn, Co, and O elements (Figure 5g).

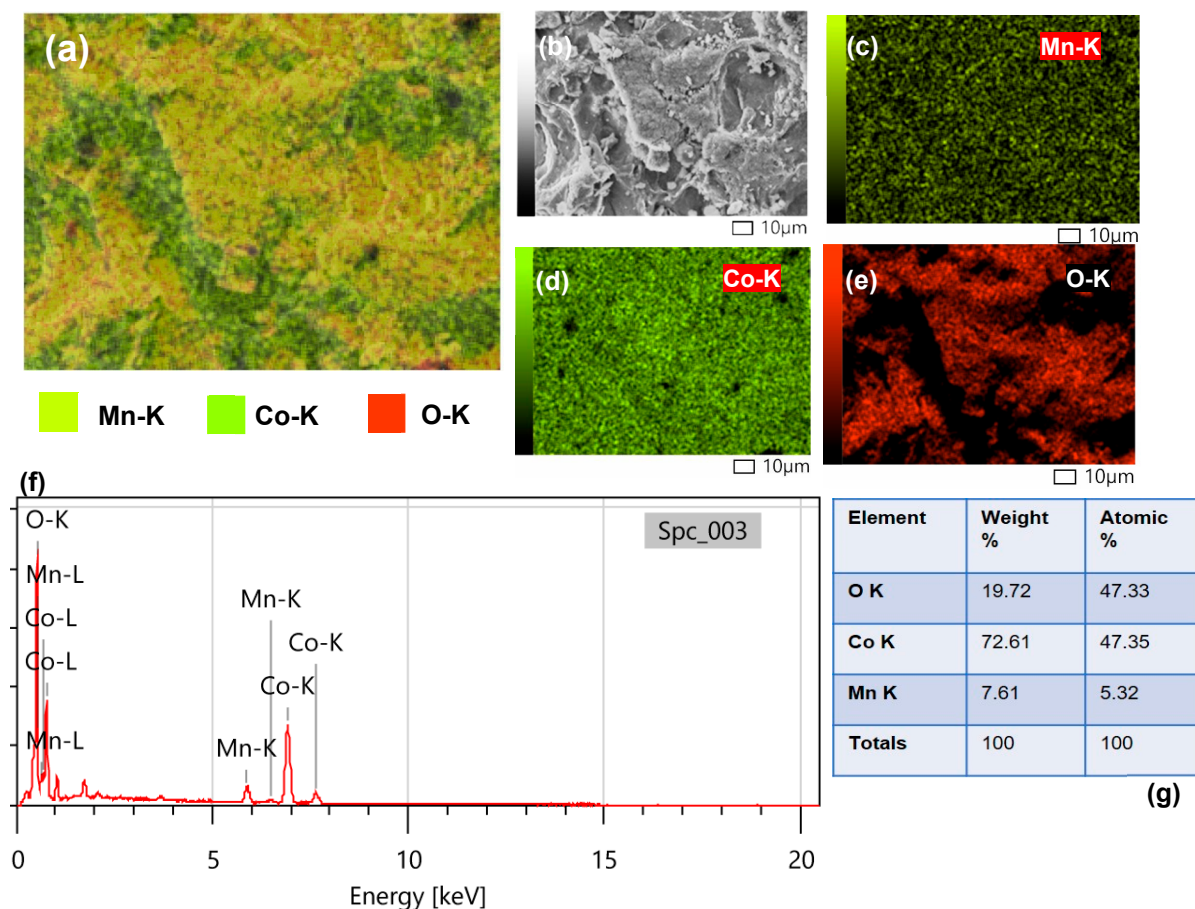


Figure 5. EDAX elemental mapping of Co, Mn, and O elements in MnCo-OOH. SEM and EDAX profiles of Mn, Co, and O elements in MnCo-OOH (a–g).

2.2. Electrochemical Performance of MnCo-OOH for OER

In Figure 6, LSV in alkaline media was used to determine the electrocatalytic features of OER materials. In a three-electrode system, $\text{Mn}(\text{OH})_2$, CoOOH , and MnCo-OOH-loaded glassy carbon electrodes were engaged as working electrodes. Figure 6a illustrates the LSV activities of bare CoOOH , bare $\text{Mn}(\text{OH})_2$, state-of-the-art IrO_2 , and MnCo-OOH electrodes in 1.0 M KOH. The LSV showed that the as-prepared Co-based electrocatalysts exhibited $\text{Co}^{2+}/\text{Co}^{3+}$ oxidation between 1.35 and 1.48 V vs. RHE [44,45]. Additionally, MnCo-OOH-loaded electrodes were the best-optimized electrode candidates for OER, with enhanced current density between 1.50 and 1.6 V compared to RHE electrodes. In electrocatalysis, the onset potential can be roughly determined by measuring the x-coordinate of the point where the two linear parts cross. Additionally, the MnCo-OOH catalyst's OER onset potential was shifted by about 90 mV to a more negative position than the bare CoOOH catalyst, showing much faster OER kinetics. As seen in Figure 6b, the Tafel slope of MnCo-OOH (99 mV dec^{-1}) is suggestively lesser than those of IrO_2 (115 mV dec^{-1}), and CoOOH (64 mV dec^{-1}). Based on the smaller Tafel slope for MnCo-OOH compared to $\text{Mn}(\text{OH})_2$, it is evident that the simultaneous influence of co-doped Mn and Co elements significantly enhances the electrochemical kinetics of OER [46].

An ECSA was employed in order to examine the effect of Mn incorporation on the enhancement of Mn-CoOOH catalysts towards OER activity. The capacitive currents revealed in Figure 6c of the obtained electrode materials demonstrate that the linear slope for the attained catalysts, CoOOH and MnCo-OOH, is 44.05 and 64.4 mF cm^{-2} , correspondingly. Based on the results, MnCo-OOH catalysts have a larger ECSA compared to catalysts without Mn incorporation, confirming that Mn generates more active sites. Among all fabricated electrodes, MnCo-OOH catalysts have the best performance (Figure 6c). The

OER features of electrocatalysts are enhanced with increased Mn loading in alkaline conditions. An MnCo-OOH catalyst exhibits the best electrocatalysis performance among the synthesized CoOOH, IrO₂, and MnCo-OOH catalysts (Figure 6d), with a lower onset potential and an overpotential of 259 mV.

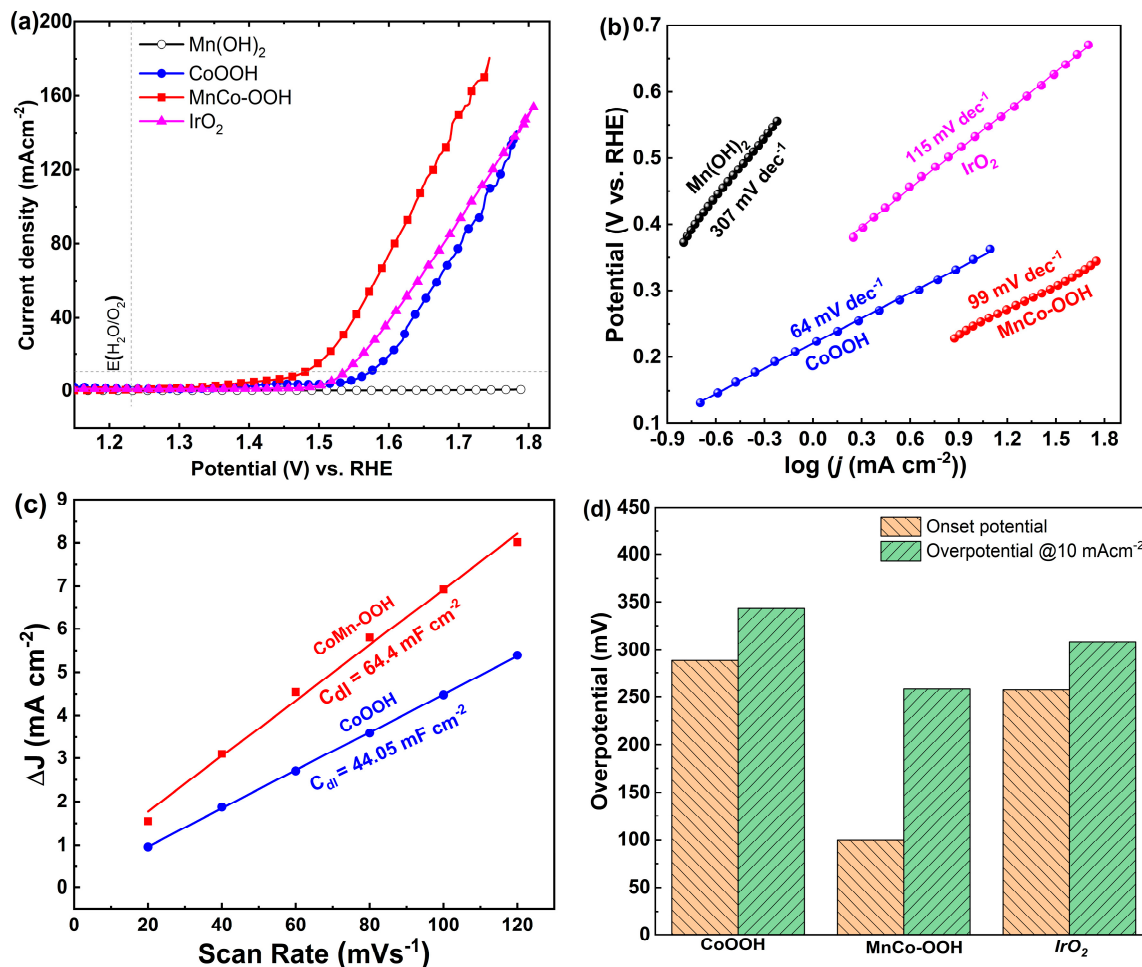


Figure 6. Electrochemical OER characteristics of films. (a) LSV plots of Mn(OH)₂, CoOOH, and MnCo-OOH materials on GC substrate in 1.0 M KOH at 10 mV s⁻¹. (b) Tafel curves acquired from the LSV plots in (a). (c) Linear curves of capacitive currents of the obtained electrodes against scan rate. (d) A comparison of catalyst OER properties and current properties at varied potentials.

To gain a better quantitative understanding of the OER process, we studied the kinetics and charge transfer process using EIS. In Figure 7, Nyquist plots are shown for pure CoOOH and MnCo-OOH electrodes at 1.48 V (vs. RHE), and impedance parameters are shown in Table 2. In Figure 7a, the Nyquist plots best match Randle's equivalent circuits. In Figure 7b, the same data are also plotted in Bode format. It is confirmed that the RCT of the catalysts examined corresponds to the lower frequency zone and its equivalent circuit. After Mn was introduced into a CoOOH framework, R1 and R2 values decreased. As shown in Table 2, the MnCo-OOH, CoOOH, and Mn(OH)₂ R2 values are 8.32, 31.45, and 4154 Ω, respectively. Most noticeably, the arc radius of the Nyquist curve of MnCo-OOH electrodes is smaller than that of CoOOH electrodes. Accordingly, MnCo-OOH has smaller R2 values, indicating more significant electrochemical features, as described earlier. Similarly, MnCo-OOH electrodes in Figure 7b show lower resistance than CoOOH electrodes in Bode plots. MnCo-OOH has an excellent charge transfer capability, which contributes to the electrode's higher intrinsic OER properties. It has been demonstrated that ternary transition

metal oxides are best formed using doping approaches, and that Mn's synergetic effect on CoOOH integration greatly enhances the performance of the OER electrocatalytic system.

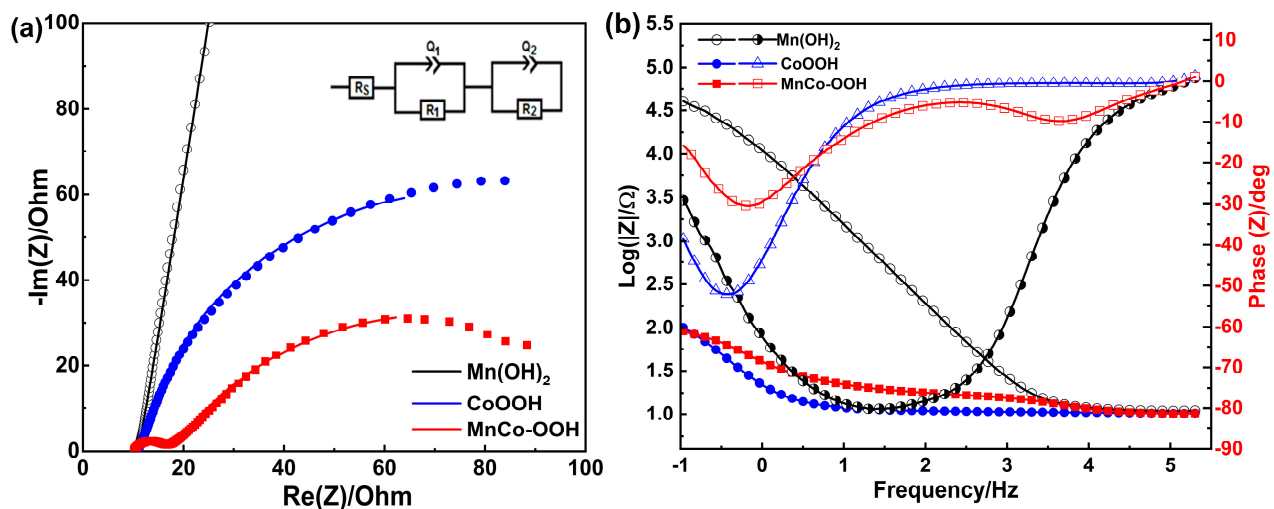


Figure 7. Nyquist plots of electrodes (a) and phase angle plots (b) derived from EIS analysis in 1.0 M KOH at 1.48 V_{RHE} of bare Mn(OH)₂, CoOOH and MnCo-OOH catalysts.

Table 2. EIS parameters were used to calculate equivalent circuits of impedance spectra in 1.0 M KOH solutions. R_s = solution resistance, R₁ = film resistance, R₂ = charge-transfer resistance, Q₁ = CPE of electrode layer, Q₂ signifies the double layer capacitance.

Samples	R _s (ohm)	Q ₁ (μF)	R ₁ (ohm)	Q ₂ (μF)	R ₂ (ohm)
Mn(OH) ₂	10.96	17.63	27,365	42.24	4154
CoOOH	10.28	8842	126	16,520	31.45
MnCo-OOH	9.84	11,830	105	33,500	8.32

The durability of OER on MnCo-OOH was investigated using CA measurements at 1.55 V vs. RHE in 1.0 M KOH. Additionally, CoOOH (Figure 8a) and MnCo-OOH (Figure 8b) samples were also tested for 12 h under a nearly constant voltage of 1.55 V_{RHE} and 1.60 V_{RHE} in alkaline mediums. During the electrochemical reaction, when a sufficient voltage is applied, oxygen gas is produced at the electrode surface. The oxygen ions then combine to form oxygen bubbles, which detach from the electrode and rise to the surface. In particular, at 1.60 V compared to RHE, oxygen bubbles at the electrode surface are definitely responsible for the fluctuations in current. According to the results, MnCo-OOH electrodes maintain a nearly constant current density over a long period of time. In comparison with other MnCo-OOH catalysts, CoOOH exhibited much lower CA currents and the acquired results agree with the LSV curve (Figure 6a). After calcination, MnCo-OOH electrodes create metal oxide networks that make them suitable for OER because they can be transported easily, have high electronic conductivity, and can be transported in mass [47]. Furthermore, MnCo-OOH electrodes show good durability and stability, with no sign of degradation even after 12 h of operation. Ultimately, MnCo-OOH electrodes prove to be a promising and cost-efficient choice for OER applications. In Table 3, we compared the electrocatalytic properties of MnCo-OOH@GC with those of other catalysts found in the literature. In particular, our catalyst exhibited a significantly higher OER activity, achieving a lower overpotential and a higher current density. Due to its improved OER features, MnCo-OOH@GC electrode materials offer great potential for energy storage and conversion systems.

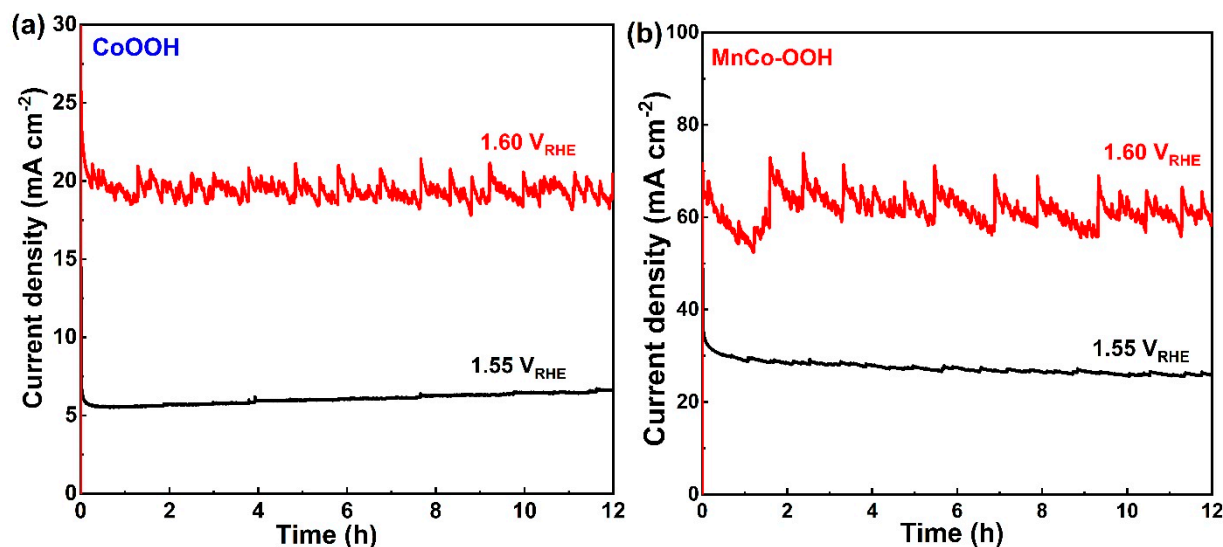


Figure 8. Durability tests. Chronoamperometry responses of CoOOH (a) and MnCo-OOH (b) electrocatalysts evaluated in 1.0 M KOH at 1.55 V vs. RHE and 1.60 V vs. RHE.

Table 3. Comparison of our catalyst MnCo-OOH electrochemical performance with those published for Mn/Co-based catalysts in alkaline medium.

Anodic Catalysts	Overpotential at 10 mA·cm ^{−2} , mV	Current Density, mA·cm ^{−2} at 1.6 V _{RHE}	Tafel Slope, mV·dec ^{−1}	Electrolyte Conc., M	Ref.
5%Ni-Co@PG carbon	381	48	73	0.1 M KOH	[48]
Cu-doped Co(OH) ₂ nanosheets@GC	300	102	47	1.0 M KOH	[49]
Ni-doped Co ₃ O ₄ @GC	380	-	63	1.0 M KOH	[50]
Ni/Ni _{0.2} Mo _{0.8} N/MoO ₃ @NF	318	75	100	1.0 M KOH	[51]
Fe-CoOOH/G @GC	330	25	37	1.0 M KOH	[52]
Fe _{0.33} Co _{0.67} OOH PNSAs@CFC	266	-	30	1.0 M KOH	[53]
Cu-CoOOH@CFP	234	-	79	1.0 M KOH	[54]
FeV/m-Co ₃ S ₄ @GC	280	63	41	1.0 M KOH	[55]
Ce-doped NiCo LDH@NF	236	-	44	1.0 M KOH	[56]
WCoO-NP@GC	270	44	92	1.0 M KOH	[57]
MnCo-OOH@GC	250	78	99	1.0 M KOH	This work

PG—pyrolytic graphite carbon electrode; CFC—carbon fiber paper; NF—nickel foam; GC—glassy carbon.

3. Experimental Methods

3.1. Materials

Cobalt (II) nitrate hexahydrate (Co(NO₃)₂·6H₂O, ≥98.0%), manganese dichloride (MnCl₂, ≥98.0%), and sodium hydroxide (NaOH, ≥85.8%) were acquired from Fisher Scientific, Hampton, NH, USA. Potassium hydroxide (KOH, ≥84.5%) was obtained from Pan-Raeac AppliChem, Darmstadt, Germany. All chemicals were used without any modification.

3.2. Preparation of Alkanna Tinctorial Root Extract

To remove impurities, alkanna dye root was washed several times with deionized (DI) water. In total, 10 g of alkanna tinctorial root was heated in 100 mL of DI water at 60 °C for 3 h. The aqueous extract was filtered. The filtration was used as a reducing agent.

3.3. Preparation of Co/Mn Oxide Nanoparticles Synthesis

A total of 100 mL of 0.02 M $\text{Co}_3(\text{NO}_3)_2 \cdot 6\text{H}_2\text{O}$ and 0.002 M MnCl_2 were mixed with 20 mL of alkanna tinctorial root extract. Afterward, the reaction mixture was left to stir for three hours. The pH was maintained at 10 by adding 1 M of NaOH. The reaction left to continue stirring for 3 h. The nanoparticles were collected using a Buckner funnel. The product was washed several times with DI water to remove impurities. Afterwards, the acquired product was calcined at 200 °C for three hours. As control catalysts, CoOOH and MnOOH samples were prepared using the same steps, but in the presence of Mn or Co precursors.

3.4. Catalyst Characterization

The crystalline nature of the materials was evaluated with XRD on a Bruker D8-advance diffractometer ($\lambda = 1.5418 \text{ \AA}$) (Bruker, Ettlingen, Germany). Using linear sweep voltammetry, chronoamperometry, and EIS, we measured the electrochemical characteristics of the obtained materials using a three-electrode Pyrex glass cell with a computerized potentiostat/galvanostat (Autolab, Bloomfield Hills, MI, USA, PGSTAT30). A Pt counter electrode and an Ag/AgCl (3.0M KCl) reference electrode were employed, while glassy carbon supported catalysts were engaged as working electrodes. As a reference electrode, an Ag/AgCl (1 M KCl) reference electrode was used, which was modified according to Nernst equation to obtain the reversible hydrogen electrode (RHE). OER was conducted at 25 °C with 1.0 M KOH at a sweep rate of 10 mVs^{-1} . Using the electrode materials at fixed potentials, CA characterization was performed in order to determine their durability.

4. Conclusions

We developed a simple green synthetic method for ternary manganese-integrated CoOOH electrocatalysts. Further, the resulting MnCo-OOH catalyst displayed excellent OER performance and reduced charge transfer resistance. MnCo-OOH composite electrodes also demonstrated better conductivity, electrocatalytic activity, and stability than CoOOH electrocatalysts and benchmark IrO_2 electrocatalysts. The electrocatalytic properties of MnCo-OOH are attributed to its high electronic conductivity, allowing rapid reaction reactants and product diffusion and interfacial electron transport. As a result of these results, we demonstrated the importance of green synthetic approaches in the preparation of CoOOH-based electrocatalysts that demonstrate electrochemical activity for water splitting in alkaline environments.

Author Contributions: R.A.: Conceptualization, supervision, methodology, investigation, data curation, formal analysis, project administration, funding acquisition. M.S.A.: Conceptualization, data curation, formal analysis writing—review and editing. P.A.: Writing—review and editing, data curation. S.G.A.: Data curation, formal analysis. All authors have read and agreed to the published version of the manuscript.

Funding: This research was supported by the Researchers Supporting Project number (RSPD2024R644) at King Saud University, Riyadh, Saudi Arabia.

Data Availability Statement: All data generated or analyzed during this study are included in this published article.

Conflicts of Interest: The authors declare no conflict of interest.

References

1. Suen, N.T.; Hung, S.F.; Quan, Q.; Zhang, N.; Xu, Y.J.; Chen, H.M. Electrocatalysis for the oxygen evolution reaction: Recent development and future perspectives. *Chem. Soc. Rev.* **2017**, *46*, 337–365. [[CrossRef](#)] [[PubMed](#)]
2. Burke, M.S.; Enman, L.J.; Batchellor, A.S.; Zou, S.; Boettcher, S.W. Oxygen evolution reaction electrocatalysis on transition metal oxides and (oxy) hydroxides: Activity trends and design principles. *Chem. Mater.* **2015**, *27*, 7549–7558. [[CrossRef](#)]
3. Zhang, Y.L.; Goh, K.; Zhao, L.; Sui, X.L.; Gong, X.F.; Cai, J.J.; Wang, Z.B. Advanced non-noble materials in bifunctional catalysts for ORR and OER toward aqueous metal–air batteries. *Nanoscale* **2020**, *12*, 21534–21559. [[CrossRef](#)] [[PubMed](#)]

4. Xie, J.; Zhang, J.; Li, S.; Grote, F.; Zhang, X.; Zhang, H.; Wang, R.; Lei, Y.; Pan, B.; Xie, Y. Controllable disorder engineering in oxygen-incorporated MoS₂ ultrathin nanosheets for efficient hydrogen evolution. *J. Am. Chem. Soc.* **2013**, *135*, 17881–17888. [\[CrossRef\]](#) [\[PubMed\]](#)
5. Safizadeh, F.; Ghali, E.; Houlachi, G. Electrocatalysis developments for hydrogen evolution reaction in alkaline solutions—A review. *Int. J. Hydrogen Energy* **2015**, *40*, 256–274. [\[CrossRef\]](#)
6. Ramakrishnan, S.; Balamurugan, J.; Vinothkannan, M.; Kim, A.R.; Sengodan, S.; Yoo, D.J. Nitrogen-doped graphene encapsulated FeCoMoS nanoparticles as advanced trifunctional catalyst for water splitting devices and zinc–air batteries. *Appl. Catal. B Environ.* **2020**, *279*, 119381. [\[CrossRef\]](#)
7. Zhai, Y.; Ren, X.; Yan, J.; Liu, S. High density and unit activity integrated in amorphous catalysts for electrochemical water splitting. *Small Struct.* **2021**, *2*, 2000096. [\[CrossRef\]](#)
8. Rani, K.K.; Karuppiyah, C.; Wang, S.F.; Alaswad, S.O.; Sireesha, P.; Devasenathipathy, R.; Jose, R.; Yang, C.C. Direct pyrolysis and ultrasound assisted preparation of N, S co-doped graphene/Fe₃C nanocomposite as an efficient electrocatalyst for oxygen reduction and oxygen evolution reactions. *Ultrason. Sonochemistry* **2020**, *66*, 105111. [\[CrossRef\]](#) [\[PubMed\]](#)
9. Atchudan, R.; Edison, T.N.J.I.; Perumal, S.; Vinodh, R.; Muthuchamy, N.; Lee, Y.R. One-pot synthesis of Fe₃O₄@graphite sheets as electrocatalyst for water electrolysis. *Fuel* **2020**, *277*, 118235. [\[CrossRef\]](#)
10. Audichon, T.; Napporn, T.W.; Canaff, C.; Morais, C.; Comminges, C.; Kokoh, K.B. IrO₂ coated on RuO₂ as efficient and stable electroactive nanocatalysts for electrochemical water splitting. *J. Phys. Chem. C* **2016**, *120*, 2562–2573. [\[CrossRef\]](#)
11. Amer, M.S.; Ghanem, M.A.; Al-Mayouf, A.M.; Arunachalam, P. Low-symmetry mesoporous titanium dioxide (Ism-TiO₂) electrocatalyst for efficient and durable oxygen evolution in aqueous alkali. *J. Electrochem. Soc.* **2018**, *165*, H300. [\[CrossRef\]](#)
12. Amer, M.S.; Arunachalam, P.; Al-Mayouf, A.M.; AlSaleh, A.A.; Almutairi, Z.A. Bifunctional vanadium doped mesoporous Co₃O₄ on nickel foam towards highly efficient overall urea and water splitting in the alkaline electrolyte. *Environ. Res.* **2023**, *236*, 116818. [\[CrossRef\]](#)
13. ben Gubaer, S.O.; Shaddad, M.N.; Arunachalam, P.; Amer, M.S.; Aladeemy, S.A.; Al-Mayouf, A.M. Enhanced electrocatalytic oxygen redox reactions of iron oxide nanorod films by combining oxygen vacancy formation and cobalt doping. *RSC Adv.* **2023**, *13*, 33242–33254. [\[CrossRef\]](#)
14. Chen, D.; Sun, Q.; Han, C.; Guo, Y.; Huang, Q.; Goddard, W.A.; Qian, J. Enhanced oxygen evolution catalyzed by in situ formed Fe-doped Ni oxyhydroxides in carbon nanotubes. *J. Mater. Chem. A* **2022**, *10*, 16007–16015. [\[CrossRef\]](#)
15. Guo, Y.; Huang, Q.; Ding, J.; Zhong, L.; Li, T.-T.; Pan, J.; Hu, Y.; Qian, J.; Huang, S. CoMo carbide/nitride from bimetallic MOF precursors for enhanced OER performance. *Int. J. Hydrogen Energy* **2021**, *46*, 22268–22276. [\[CrossRef\]](#)
16. Abdelghafar, F.; Xu, X.; Jiang, S.P.; Shao, Z. Perovskite for electrocatalytic oxygen evolution at elevated temperatures. *ChemSusChem* **2024**, e202301534. [\[CrossRef\]](#)
17. Xu, X.; Pan, Y.; Ge, L.; Chen, Y.; Mao, X.; Guan, D.; Li, M.; Zhong, Y.; Hu, Z.; Peterson, V.K.; et al. High-performance perovskite composite electrocatalysts enabled by controllable interface engineering. *Small* **2021**, *17*, 2101573. [\[CrossRef\]](#) [\[PubMed\]](#)
18. Jung, S.; McCrory, C.C.; Ferrer, I.M.; Peters, J.C.; Jaramillo, T.F. Benchmarking nanoparticulate metal oxide electrocatalysts for the alkaline water oxidation reaction. *J. Mater. Chem. A* **2016**, *4*, 3068–3076. [\[CrossRef\]](#)
19. Lewis, N.S. Research opportunities to advance solar energy utilization. *Science* **2016**, *351*, aad1920. [\[CrossRef\]](#)
20. Sun, H.; Hu, X.; Shao, Z.; Jung, W. Advanced electrocatalysts with unusual active sites for electrochemical water splitting. *InfoMat* **2024**, *6*, e12494. [\[CrossRef\]](#)
21. Elizarova, G.L.; Zhidomirov, G.M.; Parmon, V.N. Hydroxides of transition metals as artificial catalysts for oxidation of water to dioxygen. *Catal. Today* **2000**, *58*, 71–88. [\[CrossRef\]](#)
22. Decrée, S.; Pourret, O.; Baele, J.M. Rare earth element fractionation in heterogenite (CoOOH): Implication for cobalt oxidized ore in the Katanga Copperbelt (Democratic Republic of Congo). *J. Geochem. Explor.* **2015**, *159*, 290–301. [\[CrossRef\]](#)
23. Wu, R.J.; Wu, J.G.; Tsai, T.K.; Yeh, C.T. Use of cobalt oxide CoOOH in a carbon monoxide sensor operating at low temperatures. *Sens. Actuators B Chem.* **2006**, *120*, 104–109. [\[CrossRef\]](#)
24. Hou, X.G.; Liu, W.W.; Li, C.X.; Wang, Y.F. Preparation and study of spherical nickel hydroxide coated by cobalt oxy-hydroxide. *Adv. Mater. Res.* **2013**, *668*, 383–387. [\[CrossRef\]](#)
25. Fu, X.Z.; Xu, Q.C.; Hu, R.Z.; Pan, B.X.; Lin, J.D.; Liao, D.W. β-CoOOH coated spherical β-NiOOH as the positive electrode material for alkaline Zn-NiOOH battery. *J. Power Sources* **2007**, *164*, 916–920. [\[CrossRef\]](#)
26. Dhawale, D.S.; Kim, S.; Park, D.H.; Choy, J.H.; Al-Deyab, S.S.; Ariga, K.; Kim, E.; Vinu, A. Hierarchically ordered porous CoOOH thin-film electrodes for highperformance supercapacitors. *ChemElectroChem* **2015**, *2*, 497–502. [\[CrossRef\]](#)
27. Wu, Z.; Wang, X.; Huang, J.; Gao, F. A Co-doped Ni-Fe mixed oxide mesoporous nanosheet array with low overpotential and high stability towards overall water splitting. *J. Mater. Chem. A* **2018**, *6*, 167–178. [\[CrossRef\]](#)
28. Amer, M.S.; AGhanem, M.; Arunachalam, P.; M Al-Mayouf, A.; A Aljohani, T. Modification of mesoporous titanium dioxide with cobalt oxide electrocatalyst for enhanced oxygen evolution reaction. *Adv. Mater. Lett.* **2019**, *10*, 136–144. [\[CrossRef\]](#)
29. Amer, M.S.; Arunachalam, P.; Ghanem, M.A.; Al-Shalwi, M.; Ahmad, A.; Alharthi, A.I.; Al-Mayouf, A.M. Synthesis of iron and vanadium co-doped mesoporous cobalt oxide: An efficient and robust catalysts for electrochemical water oxidation. *Int. J. Energy Res.* **2021**, *45*, 9422–9437. [\[CrossRef\]](#)
30. Zhong, D.; Zhang, L.; Li, C.; Li, D.; Wei, C.; Zhao, Q.; Li, J.; Gong, J. Nanostructured NiFe (oxy) hydroxide with easily oxidized Ni towards efficient oxygen evolution reactions. *J. Mater. Chem. A* **2018**, *6*, 16810–16817. [\[CrossRef\]](#)

31. Friebe, D.; Louie, M.W.; Bajdich, M.; Sanwald, K.E.; Cai, Y.; Wise, A.M.; Cheng, M.-J.; Sokaras, D.; Weng, T.-C.; Alonso-Mori, R.; et al. Identification of highly active Fe sites in (Ni, Fe) OOH for electrocatalytic water splitting. *J. Am. Chem. Soc.* **2015**, *137*, 1305–1313. [\[CrossRef\]](#) [\[PubMed\]](#)
32. Bates, M.K.; Jia, Q.; Doan, H.; Liang, W.; Mukerjee, S. Charge-transfer effects in Ni–Fe and Ni–Fe–Co mixed-metal oxides for the alkaline oxygen evolution reaction. *ACS Catal.* **2016**, *6*, 155–161. [\[CrossRef\]](#)
33. Favaro, M.; Drisdell, W.S.; Marcus, M.A.; Gregoire, J.M.; Crumlin, E.J.; Haber, J.A.; Yano, J. An operando investigation of (Ni–Fe–Co–Ce)O_x system as highly efficient electrocatalyst for oxygen evolution reaction. *ACS Catal.* **2017**, *7*, 1248–1258. [\[CrossRef\]](#)
34. Pal, G.; Rai, P.; Pandey, A. Green synthesis of nanoparticles: A greener approach for a cleaner future. In *Green Synthesis, Characterization and Applications of Nanoparticles*; Elsevier: Amsterdam, The Netherlands, 2019; pp. 1–26.
35. Jadoun, S.; Arif, R.; Jangid, N.K.; Meena, R.K. Green synthesis of nanoparticles using plant extracts: A review. *Environ. Chem. Lett.* **2021**, *19*, 355–374. [\[CrossRef\]](#)
36. Shafey, A.M.E. Green synthesis of metal and metal oxide nanoparticles from plant leaf extracts and their applications: A review. *Green Process. Synth.* **2020**, *9*, 304–339. [\[CrossRef\]](#)
37. Singh, J.; Dutta, T.; Kim, K.-H.; Rawat, M.; Samddar, P.; Kumar, P. ‘Green’ synthesis of metals and their oxide nanoparticles: Applications for environmental remediation. *J. Nanobiotechnol.* **2018**, *16*, 84. [\[CrossRef\]](#) [\[PubMed\]](#)
38. Su, L.H.; Zhang, X.G.; Mi, C.H.; Gao, B.; Liu, Y. Improvement of the capacitive performances for Co–Al layered double hydroxide by adding hexacyanoferrate into the electrolyte. *Phys. Chem. Chem. Phys.* **2009**, *11*, 2195–2202. [\[CrossRef\]](#)
39. Xu, R.; Zeng, H.C. Dimensional control of cobalt-hydroxide-carbonate nanorods and their thermal conversion to one-dimensional arrays of Co₃O₄ nanoparticles. *J. Phys. Chem. B* **2003**, *107*, 12643–12649. [\[CrossRef\]](#)
40. Han, Q.; Dong, Z.; Tang, X.; Wang, L.; Ju, Z.; Liu, W. A ratiometric nanoprobe consisting of up-conversion nanoparticles functionalized with cobalt oxyhydroxide for detecting and imaging ascorbic acid. *J. Mater. Chem. B* **2017**, *5*, 167–172. [\[CrossRef\]](#) [\[PubMed\]](#)
41. Chen, H.; He, J. Facile synthesis of monodisperse manganese oxide nanostructures and their application in water Treatment. *J. Phys. Chem. C* **2008**, *112*, 17540–17545. [\[CrossRef\]](#)
42. Wang, H.; Gao, Q.; Jiang, L. Facile approach to prepare nickel cobaltite nanowire materials for supercapacitors. *Small (Weinheim, Bergstr. Ger.)* **2011**, *7*, 2454–2459. [\[CrossRef\]](#)
43. Sakatani, Y.; Grosso, D.; Nicole, L.; Boissière, C.; de AA Soler-Illia, G.J.; Sanchez, C. Optimised photocatalytic activity of grid-like mesoporous TiO₂ films: Effect of crystallinity, pore size distribution, and pore accessibility. *J. Mater. Chem.* **2006**, *16*, 77–82. [\[CrossRef\]](#)
44. Boggio, R.; Carugati, A.; Trasatti, S. Electrochemical surface properties of Co₃O₄ electrodes. *J. Appl. Electrochem.* **1987**, *17*, 828–840. [\[CrossRef\]](#)
45. Leng, X.; Zeng, Q.; Wu, K.H.; Gentle, I.R.; Wang, D.W. Reduction-induced surface amorphization enhances the oxygen evolution activity in Co₃O₄. *RSC Adv.* **2015**, *5*, 27823–27828. [\[CrossRef\]](#)
46. Burke, M.S.; Kast, M.G.; Trotochaud, L.; Smith, A.M.; Boettcher, S.W. Cobalt–iron (oxy) hydroxide oxygen evolution electrocatalysts: The role of structure and composition on activity, stability, and mechanism. *J. Am. Chem. Soc.* **2015**, *137*, 3638–3648. [\[CrossRef\]](#)
47. Trześniewski, B.J.; Diaz-Morales, O.; Vermaas, D.A.; Longo, A.; Bras, W.; Koper, M.T.; Smith, W.A. In situ observation of active oxygen species in Fe-containing Ni-based oxygen evolution catalysts: The effect of pH on electrochemical activity. *J. Am. Chem. Soc.* **2015**, *137*, 15112–15121. [\[CrossRef\]](#) [\[PubMed\]](#)
48. Song, W.; Ren, Z.; Chen, S.-Y.; Meng, Y.; Biswas, S.; Nandi, P.; A Elsen, H.; Gao, P.-X.; Suib, S.L. Ni-and Mn-promoted mesoporous Co₃O₄: A stable bifunctional catalyst with surface-structure-dependent activity for oxygen reduction reaction and oxygen evolution reaction. *ACS Appl. Mater. Interfaces* **2016**, *8*, 20802–20813. [\[CrossRef\]](#) [\[PubMed\]](#)
49. Chen, L.; Zhang, H.; Chen, L.; Wei, X.; Shi, J.; He, M. Facile synthesis of Cu doped cobalt hydroxide (Cu–Co (OH)₂) nano-sheets for efficient electrocatalytic oxygen evolution. *J. Mater. Chem. A* **2017**, *5*, 22568–22575. [\[CrossRef\]](#)
50. Vazhayil, A.; Thomas, N. Probing the electrocatalytic activity of hierarchically mesoporous M–Co₃O₄ (M = Ni, Zn, and Mn) with branched pattern for oxygen evolution reaction. *J. Electroanal. Chem.* **2023**, *934*, 117298. [\[CrossRef\]](#)
51. Li, R.-Q.; Li, S.X.; Lu, M.J.; Shi, Y.Q.; Qu, K.G.; Zhu, Y.C. Energy-Efficient Hydrogen Production over A High-Performance Bifunctional NiMo-based Nanorods Electrode. *J. Colloid Interface Sci.* **2020**, *571*, 48–54. [\[CrossRef\]](#)
52. Han, X.; Yu, C.; Zhou, S.; Zhao, C.; Huang, H.; Yang, J.; Liu, Z.; Zhao, J.; Qiu, J. Ultrasensitive iron-triggered nanosized Fe–CoOOH integrated with graphene for highly efficient oxygen evolution. *Adv. Energy Mater.* **2017**, *7*, 1602148. [\[CrossRef\]](#)
53. Ye, S.H.; Shi, Z.X.; Feng, J.X.; Tong, Y.X.; Li, G.R. Activating CoOOH porous nanosheet arrays by partial iron substitution for efficient oxygen evolution reaction. *Angew. Chem. Int. Ed.* **2018**, *57*, 2672–2676. [\[CrossRef\]](#) [\[PubMed\]](#)
54. Yan, L.; Zhang, B.; Liu, Z.; Zhu, J. Synergy of copper doping and oxygen vacancies in porous CoOOH nanoplates for efficient water oxidation. *Chem. Eng. J.* **2021**, *405*, 126198. [\[CrossRef\]](#)
55. Amer, M.S.; Arunachalam, P.; Al-Mayouf, A.M.; Alsaleh, A.A.; Alshalwi, M.; AAlmutairi, Z. Effect of Iron and Vanadium Doping on Structural Phase Transition in Cobalt Diselenide Enabling Superior Oxygen/Hydrogen Electrocatalysis. *ACS Appl. Energy Mater.* **2023**, *6*, 11718–11731. [\[CrossRef\]](#)

56. He, Y.; Wang, Y.; Wang, X.; Lu, W.; Yu, T.; Luo, Y.; Ding, H.; Chen, L. Ce-Induced Morphology Evolution and Electronic Structure Modulation of NiCo Layered Double Hydroxides for Efficient Oxygen Evolution Catalysis. 2023. Available online: https://papers.ssrn.com/sol3/papers.cfm?abstract_id=4653890 (accessed on 1 June 2024).
57. Amer, M.S.; Arunachalam, P.; Ghanem, M.A.; Al-Mayouf, A.M.; Shar, M.A. Enriched active surface structure in nanosized tungsten-cobalt oxides electrocatalysts for efficient oxygen redox reactions. *Appl. Surf. Sci.* **2020**, *513*, 145831. [[CrossRef](#)]

Disclaimer/Publisher's Note: The statements, opinions and data contained in all publications are solely those of the individual author(s) and contributor(s) and not of MDPI and/or the editor(s). MDPI and/or the editor(s) disclaim responsibility for any injury to people or property resulting from any ideas, methods, instructions or products referred to in the content.